Published online 1 March 2019

Nucleic Acids Research, 2019, Vol. 47, No. 7 **3295–3305**
doi: 10.1093/nar/gkz135

Submolecular dissection reveals strong and specific binding of polyamide–pyridostatin conjugates to human telomere interface

Shankar Mandal[1], Yusuke Kawamoto[2], Zhizhou Yue[1], Kaori Hashiya[2], Yunxi Cui[1,3], Toshikazu Bando[2], Shankar Pandey[1], Mohammed Enamul Hoque[1], Mohammad Akter Hossain[1], Hiroshi Sugiyama[2,4] and Hanbin Mao[1,*]

[1]Department of Chemistry & Biochemistry, Kent State University, Kent, OH 44242, USA, [2]Department of Chemistry, Graduate School of Science, Kyoto University, Sakyo, Kyoto 606-8502, Japan, [3]State Key Laboratory of Medicinal Chemical Biology, Nankai University, 94 Weijin Road, Tianjin 300071, China and [4]Institute for Integrated Cell–Material Science (iCeMS), Kyoto University, Sakyo, Kyoto 606-8501, Japan

Received November 20, 2018; Revised February 13, 2019; Editorial Decision February 15, 2019; Accepted February 26, 2019

ABSTRACT

To modulate biological functions, G-quadruplexes in genome are often non-specifically targeted by small molecules. Here, specificity is increased by targeting both G-quadruplex and its flanking duplex DNA in a naturally occurring dsDNA–ssDNA telomere interface using polyamide (PA) and pyridostatin (PDS) conjugates (PA-PDS). We innovated a single-molecule assay in which dissociation constant (K_d) of the conjugate can be separately evaluated from the binding of either PA or PDS. We found K_d of 0.8 nM for PA-PDS, which is much lower than PDS ($K_d \sim 450$ nM) or PA ($K_d \sim 35$ nM). Functional assays further indicated that the PA-PDS conjugate stopped the replication of a DNA polymerase more efficiently than PA or PDS. Our results not only established a new method to dissect multivalent binding into actions of individual monovalent components, they also demonstrated a strong and specific G-quadruplex targeting strategy by conjugating highly specific duplex-binding molecules with potent quadruplex ligands.

INTRODUCTION

It has been demonstrated that mechanical stability of G-quadruplexes (1,2) is higher than the stall force of motor proteins such as RNA and DNA polymerases (3–5). This suggests that G-quadruplexes can interfere with replication or transcription processes from mechanical perspective. Telomeric G-quadruplex structures stabilized by a small molecule have shown increased mechanical stabilities that may further thwart the efforts of motor proteins including helicase (6–8) to work on the telomere overhang. Various G-quadruplex (GQ) targeting ligands, such as pyridostatin (PDS), have been reported by different groups (9–12). However, none of the ligands tested so far has shown strong specificity towards a particular G-quadruplex. The challenge of using small molecules to target a particular G-quadruplex arises as 716310 potential G-quadruplex forming sequences are known to exist in human genome (13,14). The situation becomes even more complicated as thousands of mRNA pieces also contain G-quadruplex forming sequences (15). Most small molecules bind to G-quadruplexes through generic π-π stacking and electrostatic attractions. However, it may be challenging to develop highly specific G-quadruplex ligands to target a particular G-quadruplex in genome to avoid non-specific binding that leads to altered expression of unrelated genes (16).

The specificity problem for G-quadruplex can be addressed by targeting the adjacent duplex DNA sequences, which are often unique (17,18). It is conceivable that by incorporating both dsDNA and G-quadruplex recognition elements in the same molecule, additive binding enthalpies will lead to stronger binding. In addition, the proximity effect in the dual recognition can reduce the entropic penalty due to the formation of the bound complex. Similar effect has been observed in the polyvalent binding that has significantly increased binding affinity relative to the monomeric recognitions (19,20).

Many approaches exist to specifically target duplex DNA. A notable example is pyrrole–imidazole polyamide (21), in which antiparallel arrangement of imidazole (Im) and pyrrole (Py) can recognize a G-C base pair, whereas a Py–Py binds to an A–T or a T–A base pair (22). Prior research has shown that different structures of polyamides, such as monomeric hairpins and cyclic/tandem hairpins (23–25), can bind to the minor groove of desired dsDNA segments found in telomere or promoter regions.

*To whom correspondence should be addressed. Tel: +1 330 672 9380; Fax: +1 330 672 3816; Email: hmao@kent.edu

Telomeres located at the end of the chromosomes are important to stabilize chromosomes and regulate replication processes (26,27). Human telomere consists of ∼10 kb duplex DNA that extends to 200 ± 75 nt single-stranded overhang at the 3′ end. Both regions contain tandem repeats of 5′-TTAGGG-3′, which are known to form G-quadruplex structures (26,28,29). The unique topology at the junction of the duplex and single-stranded telomere region offers an opportunity to specifically target the G-quadruplex formed at the interface (30). In the present study, we synthesized tandem-hairpin Py–Im polyamide–pyridostatin (PA−PDS) conjugates (Figures 1 and Supplementary Figure S1) to target natural human telomere interfaces, which were constructed by a duplex sequence, $d(TTAGGG)_2$, followed by a single-stranded sequence, $d(TTAGGG)_4$ (Supplementary Figure S2). To evaluate the binding of the PA-PDS to these telomere interfaces, we innovated sub-molecular mechanical unfolding experiments in which bindings of the two monovalent components (PA and PDS) inside the bivalent conjugate were separately determined in optical tweezers. We found that these two-component bindings demonstrated identical dissociation constants ($K_d = 0.8$ nM) to the telomere interface. Compared to the PA or PDS alone, the PA–PDS conjugates showed specific binding to the human telomere interface with ∼50 and ∼500 times higher affinities, respectively. The tighter binding also increased the capability of PA–PDS to stall replication carried out by phi 29 DNA polymerase. As polyamides can be designed to target almost any desired duplex DNA, we anticipate this dual binding strategy provides a powerful tool to address the specificity problem for the G-quadruplexes not only in telomeres, but also in promoter regions. In addition, the new single-molecule binding assay allows a sub-molecular perspective to separately evaluate the binding efficacy of each monovalent component in a multivalent ligand.

MATERIALS AND METHODS

Materials

To synthesize the DNA constructs for laser tweezers experiments, the DNA oligomers were purchased from Integrated DNA Technologies (www.idtdna.com) and purified with denaturing polyacrylamide gel electrophoresis (PAGE). Unless specified otherwise, all enzymes were obtained from New England Biolabs (www.neb.com). Streptavidin coated and anti-digoxigenin coated polystyrene beads were purchased from Spherotech (Lake Forest, IL, USA). All chemicals including Tris-HCl and KCl were purchased from either Fisher Scientific or Sigma with purities >99.0%.

Synthesis of DNA constructs for single-molecule laser tweezers experiments

The DNA constructs for single-molecule ligand-binding investigations were prepared using a similar protocol described elsewhere (1). Briefly, to synthesize the natural telomere 4G interface construct (the **–1 nt telomere interface**, Supplementary Figure S2A), the DNA sequences comprising two 5′-TTAGGG repeats in the dsDNA section and four 5′-TTAGGG repeats in the ssDNA region of the interface (see the dsDNA–ssDNA hybrid sequence below) were sandwiched between two long dsDNA spacers (2028 bp and 2690 bp). The 2028 bp handle was prepared by PCR amplification of a pBR322 plasmid (New England Biolab, NEB) using a 5′ biotinylated primer, 5′-biotin-GCA TTA GGA AGC AGC CCA GTA GTA GG-3′(IDT, Coralville, IA, USA), to label the biotin at the 5′ end. The PCR product was digested by the XbaI restriction enzyme (NEB). The 2,028 bp handle was then ligated with the dsDNA–ssDNA hybrid, 5’ CTAG TGC ATG AGC ACG G TTAGGG TTAGGG TTAGGGTTAGGGTTAGGGTTAGGGTTA GC CAG CAA GAC GTA GCC CAG CGC GTC 3’, where underline part represents the ssDNA section (see Supplementary Table S1 for DNA sequences). This hybrid consists of an XbaI overhang at the 5′-end and an EagI overhang at the 3′-end. The 2,690 bp DNA handle was synthesized by the SacI (NEB) and EagI (NEB) digestions of a pEGFP plasmid (Clontech, Mountain View, CA, USA). This handle was subsequently labeled at the 3′ end by digoxigenin (Dig) using 18 μM Dig-dUTP (Roche) and terminal transferase (Fermentas). The final DNA construct was synthesized using T4 DNA ligase (NEB) through two-piece ligation of the 2028 and 2690 dsDNA handles. Other DNA constructs with different DNA sequences in dsDNA–ssDNA hybrid (the **0 nt telomere interface** and the **+1 nt telomere interface**) were prepared using the similar procedure as described above (see Supplementary Table S1).

To synthesize the **telomere hairpin interface** construct (Supplementary Figure S2E), an oligonucleotide 5′- CTA GTG CAT TAG GAA GCA GCC CAG TAG TAG GAA AAA AAA TT CA CC ACA -3′ (Supplementary Table S1) was annealed with an oligonucleotide 5′ TTT TTT TTC CTA CTA CTG GGC TGC TTC CTA ATG CA 3′ at 97°C for 5 min and slowly cooled to room temperature for 6 h. The small dsDNA fragment was ligated with the 2028 bp DNA handle by T4 DNA ligase (NEB) and gel purified using a kit (Midsci, St. Louis, MO, USA). On the other side of the DNA construct, an oligonucleotide 5′ GGGC TGT GG TG TT GC CAG CAA GAC GTA GCC CAG CGC GTC 3′ was annealed with an oligonucleotides 5′ GGCC GAC GCG CTG GGC TAC GTC TTG CTG GC 3′ and subsequently ligated with the 2690 bp handle and gel purified. Final DNA construct was synthesized using T4 DNA ligase (NEB) through three-piece ligation of the 2028 and 2690 dsDNA handles and the oligonucleotides, 5′ GCCC GTACG TAGGG TTAGGG TTAGGGTTAGGGTTAGGGTTT TTT CTAA CCCTAA CCCTA CGTAC3′, which contained G-quadruplex forming sequence in the loop of the hairpin (underlined part represents hairpin loop).

Laser tweezers instrumentation

Detailed description of the laser tweezers instrument has been reported elsewhere (31). In brief, a diode pumped solid-state (DPSS, 1064 nm wavelengths in continuous-wave mode, BL-106C, Spectra-physics) was used to generate P- and S-polarized laser beams for two laser traps. The position of each trap was detected separately using two position-sensitive photodetectors (DL100, Pacific Silicon Sensor). A steerable mirror (Nano-MTA, Mad City Laboratories) was used to control the S-polarized light at the plane conjugate

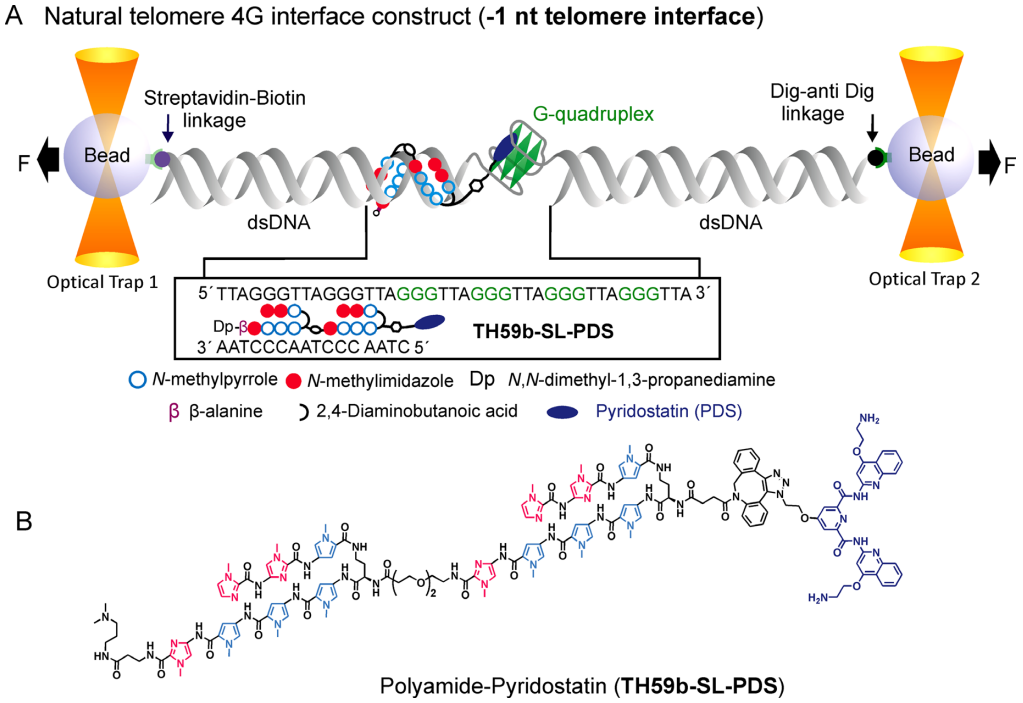

Figure 1. Schematic of the interaction between the naturally occurring human telomere interface (**–1 nt telomere interface**) and the polyamide–pyridostatin (PA–PDS) ligand. (**A**) Setup of the mechanical unfolding experiments in optical tweezers. The single-molecule platform comprises a G-quadruplex-hosting ssDNA region and a dsDNA region that binds to the tandem-hairpin pyrrole-imidazole polyamide (**TH59b-SL-PDS**, represented by empty and filled circles). This DNA interface is sandwiched between the two dsDNA spacers, which are separately tethered to the two optically trapped beads via digoxigenin (Dig) – Dig-antibody and biotin–streptavidin linkages. (**B**) Chemical structure of the tandem-hairpin pyrrole-imidazole polyamide conjugated with the pyridostatin (**TH59b-SL-PDS**).

to the back focal plane of a focusing objective (Nikon CFI-Plan-Apochromat × 60, NA = 1.2, water immersion, working distance ∼320 μm). The laser powers in the two split laser beams were maintained at 233 and 210 mW, respectively, to trap two polystyrene particles. During the experiments, the tension inside the DNA construct was exerted by the movement of the steerable mirror using the LabView 8 program (National Instruments Corporation).

Single-molecule mechanochemical experiments in a laser tweezers set up

To perform mechanochemical experiment, 1.5 μl of a diluted DNA construct (∼1 ng/μl) was incubated with 1 μl of 0.1% solution of digoxigenin (Dig)-antibody coated polystyrene beads (diameter: 2.10 μm) for about half hour at room temperature (25°C), which immobilized the DNA construct on the bead surface through the Dig-anti Dig complex formation. The incubated sample was further diluted to 1 ml in a 10 mM Tris buffer (pH 7.4, supplemented with 100 mM KCl). Streptavidin-coated polystyrene beads (1 μl, diameter: 1.87 μm) were also dispersed into the same buffer (1 ml) and injected into top two channels in a three-channel microfluidic chamber in the laser tweezers set up. The 10 mM Tris buffer (pH 7.4, supplemented with 100 mM KCl) was flowed in the middle channel of the microfluidic chamber (flow rate: 0.05 μl/min) in absence or presence of ligands. Two separate laser beams were used to trap two different types of beads. By escorting one of the trapped beads closer to another using the steerable mirror, the DNA was tethered between the two trapped beads. After the tethering, one of the trapped beads was moved away from another with a loading speed of ∼5.5 pN/s for the –1, 0 and +1 nt **telomere interface constructs** ∼1.5 pN/s for the -1 nt **hairpin telomere interface construct**. This rate allowed us to collect significant amount of data in a reasonable timescale at a condition close to the unfolding equilibrium of a DNA secondary structure. An unfolding event was identified as a sudden change in the end-to-end distance during the force ramping. The unfolding force was measured directly from the F–X curves while the change-in-contour-length (ΔL) due to the unfolding was calculated by the data points flanking the rupture event using an extensible worm-like chain (WLC) model (Equation 1) (32,33).

$$\frac{\Delta x}{\Delta L} = 1 - \frac{1}{2}\left(\frac{k_B T}{FP}\right)^{\frac{1}{2}} + \frac{F}{S} \qquad (1)$$

where Δx is the change in extension between the data points of the stretching and relaxing curves at the same force (F), k_B is the Boltzmann constant, T is absolute temperature, P is the persistent length (50.8 ± 1.5 nm) (34), and S is the elastic stretch modulus (1243 ± 63 pN) (34).

SPR assays

The SPR assays were performed on a BIACORE X instrument (GE Healthcare) with 3′–biotinylated DNA oligonucleotides (Sigma Genosis) and streptavidin–coated sensor chip SA (GE Healthcare) following the previous reports

(35–37). Sequence of the biotinylated DNA is 5′-CTAA $(CCCTAA)_2$ GCTTTTGC $(TTAGGG)_6$TTATTTT-biotin-3′. 1 nM of DNA dissolved in HBS-EP buffer (10 mM HEPES pH 7.4, 150 mM NaCl, 3 mM EDTA, 0.005% v/v Surfactant P20) was injected to immobilize the biotinylated DNA to streptavidin–coated sensor chip at a flow rate of 10 μl/min to obtain the desired immobilization level (up to ∼1000 RU rise). The assays were performed with the running buffer (10 mM HEPES pH 7.4, 200 mM KCl, 3 mM EDTA, 0.005% v/v Surfactant P20) (38) containing 0.1% DMSO at 25°C. A series of sample solutions with various concentrations were prepared in the running buffer and injected at a flow rate of 20 μl/min. After each assay, the washing buffer (1 M NaCl, 50 mM NaOH) was injected. To calculate dissociation constants (K_d), data processing of SPR sensorgrams was performed with 1:1 binding with mass transfer model using BIAevaluation 4.1 program (Supplementary Figure S15).

Polymerase stop assay

The DNA polymerase stop assay was performed according to modified protocols (39,40). Briefly, we synthesized a DNA template in which the **–1 nt telomere interface** is placed downstream of a primer labelled with Cy3 (Figure 6A). A reaction mixture (8 μl) containing the DNA template (312 nM), BSA (1×), KCl (100 mM), and ligands (78–312 nM) was incubated in a Phi29 DNA polymerase buffer (1 ×) at room temperature (25˚C) for 30 min to form G-quadruplex–ligand complex. Primer extension was carried out by adding 2 U phi29 DNA polymerase at 30˚C for 1 h. The enzymatic reaction was stopped by addition of 8 μl alkaline loading buffer (Formamide 95% and 10 mM NaOH), heated at 95˚C for 5 min, and cooled on ice for 5 min. The reaction mixture was pre-concentrated to ∼10 μl before loading for 16% denatured PAGE for 45 min at 65 W. The gel image was recorded using Typhoon FLA 9500 (GE Healthcare, Cleveland, OH, USA) and quantified using Kodak 1D Scientific Imaging System (New Haven, CT, USA). Dideoxy sequencing reactions were carried out with the same DNA template (312 nM), dNTPs (1 mM) and ddNTP (200 μM) to provide a sequencing ladder for assignment of the DNA polymerase arrest sites by adding 2.5U Taq DNA polymerase at 37˚C for 30 min.

RESULTS AND DISCUSSION

Design and synthesis of the dsDNA–ssDNA telomere interface constructs

Previous studies have shown that tandem-hairpin pyrrole–imidazole polyamides specifically recognize the telomere dsDNA with two to four repeats of 5′-TTAGGG-3′ (41–43,35,36). In our telomere interface design (Figure 1), we used two double-stranded TTAGGG repeats, which are followed by a G-quadruplex forming ssDNA, 5′-$(TTAGGG)_4$TTA-3′. Given that ∼80% of the naturally occurring double-stranded telomere ends with a C-rich sequence, 3′-CCAATC-5′ (44), we incorporated this sequence in one of our natural telomere interface constructs (Figure 1A and Supplementary Figure S2). It is noticeable that such a construct contains an overlapping G-C pair between the G-quadruplex hosting single-stranded sequence and the dsDNA segment (the construct is designated as '**-1 nt telomere interface**'), which is expected to weaken the formation of the interfacial G-quadruplex and possibly reduce the binding affinity between the pyridostatin (PDS) and the G-quadruplex. To investigate the effect of this overlapping base pair on the formation of telomere G-quadruplex, we also designed two other less abundant telomere interfaces that contain 0 and 1 base-pair spacers between the dsDNA and the G-quadruplex hosting ssDNA section (designated as '**0 nt telomere interface**' and '**+1 nt telomere interface**', respectively, see Supplementary Figure S2). The overall constructs were synthesized by sandwiching the interface sequences between two dsDNA handles of 2028 and 2690 bp in length (see Materials and Methods for details). These DNA constructs were tethered to two optically trapped beads via digoxigenin (Dig)–Dig-antibody and biotin-streptavidin linkages, respectively, for initial mechanical unfolding experiments.

Design and synthesis of the pyrrole-imidazole polyamide−pyridostatin (PA−PDS) conjugates

To evaluate the molecular binding to the telomere interfaces, three ligands were synthesized by conjugating monomeric or dimeric polyamides with the PDS (9) through different linker lengths (Supplementary Figure S1). Two of the PA−PDS conjugates (**TH59b-SL-PDS** and **TH59b-LL-PDS**) contain dimeric tandem-hairpin polyamides that are connected to the PDS via short (SL) and long (LL) linkers, respectively. The third PA−PDS conjugate (**H59-SL-PDS**) contains a monomeric hairpin polyamide that is connected to the PDS via the short linker (Supplementary Figure S1). The pyrrole-imidazole polyamides, **TH59b** and **H59**, were prepared by solid phase syntheses (see Supplementary Methods), followed by connecting to the DBCO-NHS ester with different linker lengths (Supplementary Schemes S1-S3 and Supplementary Figures S1 and S2). The final polyamide−pyridostatin conjugates (**TH59b-SL-PDS**, **TH59b-LL-PDS**, and **H59-SL-PDS**) were synthesized via copper-free click chemistry between the azide-modified PDS (see Supplementary Scheme S4 and Supplementary Methods for synthesis) and the azadibenzocyclooctyne-modified polyamides. The products were purified by HPLC and analyzed by mass spectrometry before binding experiments (Supplementary Figures S3-S9).

Strong and specific binding of the polyamide−pyridostatin conjugates to the telomere interfaces

We used the **+1 nt telomere interface** (Supplementary Figure S2B) as a single-molecule template to evaluate the binding of different PA−PDS conjugates (Supplementary Figure S1) by mechanical unfolding in optical tweezers (see Materials and Methods). First, the single-molecular DNA construct was stretched without ligand by moving one of the optically trapped beads away from another with a loading rate of 5.5 pN/s in a 10 mM Tris buffer (pH 7.4 with 100 mM KCl) at room temperature. At physiologi-

cally relevant K^+ concentration (100 mM), the telomere sequence containing four repeats of 5′TTAGGG preferentially forms hybrid-1 type (mixed parallel/antiparallel) G-quadruplex structure (Figure 1A) (45–47). As the tension inside the DNA construct increased, a rupture event was observed in the force-extension (*F–X*) curve (Supplementary Figure S10A, green) at 22.4 ± 0.8 pN (Supplementary Figure S10B, right), which indicates the unfolding of a secondary structure in the telomere interface construct. The observed change-in-contour-length (ΔL, Supplementary Figure S10B, left) during unfolding (8.0 ± 0.2 nm) matched with the expected value for unfolding of the telomeric G-quadruplex (~8.4 nm, see Supplementary Methods for calculation).

Next, the mechanical unfolding was repeated in the same buffer with 100 nM PA−PDS conjugates to investigate the ligand binding effects. We observed that in some *F–X* curves, the unfolding force increased from ~22 pN to ~45 pN (Supplementary Figure S10A, pink). The increased force is indicative of ligand binding to a telomeric G-quadruplex(1) likely (48,49). The unfolding force histograms in Supplementary Figure S10 were subsequently analyzed by statistical deconvolution (50) to obtain the fraction of ligand-bound G-quadruplex. Among the three PA−PDS conjugates (100 nM each), the dimeric tandem-hairpin polyamide−pyridostatin conjugate with a short linker (**TH59b-SL-PDS**) showed the highest bound fraction (34.4%, Supplementary Figure S10C) compared to the **H59-SL-PDS** (24.2%, Supplementary Figure S10D) or **TH59b-LL-PDS** (16.3%, Supplementary Figure S10E). Compared to the **TH59b-SL-PDS**, the less binding of the **H59-SL-PDS** can be explained by the fact that the monomeric hairpin polyamide (H59) has reduced binding specificity or affinity to the duplex telomere DNA with respect to the dimeric tandem-hairpin polyamide (TH59b). On the other hand, the low binding fraction of **TH59b-LL-PDS** to the G-quadruplex at the telomere interface can be ascribed to the long linker between the polyamide and PDS, which imparts increased entropic penalty upon the formation of the bound complex. Based on these results, in subsequent experiments we used **TH59b-SL-PDS** as the ligand to target the telomere interfaces.

To evaluate the binding of the **TH59b-SL-PDS** to the **–1 nt telomere interface** that has the highest natural abundance (44) (Figures 1 and Supplementary Figure S2A), we compared the binding of the ligand and its components, PDS and TH59b, in the same Tris buffer described above. Without ligand, we obtained a mean rupture force of 19.2 ± 0.4 pN (Figures 2A left and 2B). Similar to the TH59b-SL-PDS in the +1 nt telomere interface, in presence of 100 nM **PDS** or **TH59b-SL-PDS**, the rupture force showed two populations. While the higher force population (~40 pN, see Figure 2A right panel for a representative *F–X* curve) corresponds to the ligand-bound G-quadruplex(1), the lower force species (~20 pN) is consistent with a ligand-free G-quadruplex. After statistical deconvolution of these two populations,(50) we found that the **TH59b-SL-PDS** showed much higher bound fraction (48.8%, Figure 2C) than the **PDS** (18.7%, Figure 2D). As the **TH59b-SL-PDS** and **PDS** possess bivalent and monovalent binding modes

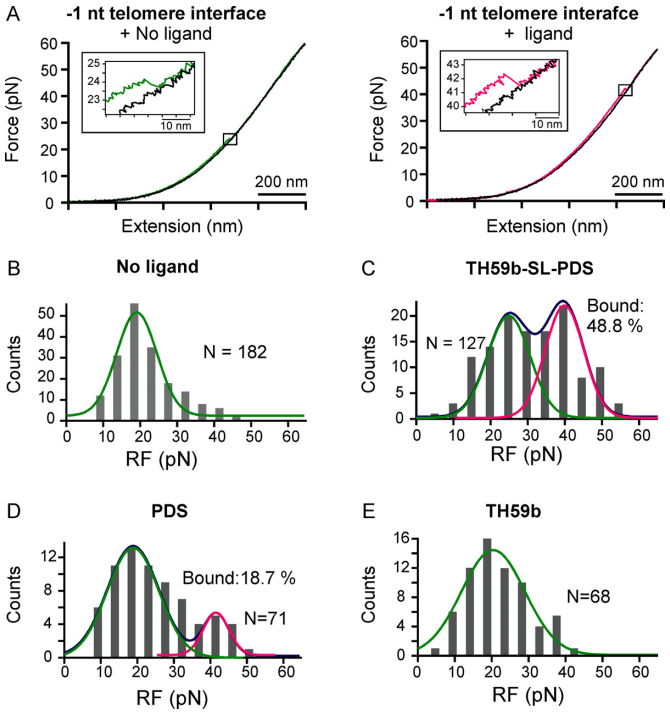

Figure 2. Typical Force-Extension (F-X) curves and unfolding force histograms of the G-quadruplex in the **–1 nt telomere interface** with and without ligands. (**A**) Representative *F–X* curves with unfolding features (insets) for the G-quadruplex in the telomere interface without (left) and with (right) 100 nM ligands in a 10 mM Tris buffer (pH 7.4) supplemented with 100 mM KCl. Colored and black traces represent stretching and relaxing curves, respectively. The rupture force (RF) histograms of the **–1 nt telomere interface** are shown in the same buffer without ligand (**B**) and with 100 nM each of **TH59b-SL-PDS** (**C**), **PDS** (**D**) and **TH59b** (**E**). The green solid curve depicts the ligand-free G-quadruplex whereas the pink solid curve represents the ligand-bound G-quadruplex. *N* represents the number of unfolding features.

respectively, this result confirmed that additive binding enthalpies and reduced entropic penalty in the bivalent binding lead to increased affinity (23). It is noteworthy that the dimeric tandem-hairpin polyamide **TH59b** did not stabilize G-quadruplex as the mean rupture force (20.1 ± 0.5 pN, Figure 2E) was similar to that without ligand (19.2 ± 0.4 pN, Figure 2B). Due to the mechanical unfolding orientation that aligns with the duplex DNA adjacent to the G-quadruplex-containing fragment (Figure 1A), we were not able to evaluate the binding of the **TH59b** to the duplex telomere DNA.

As a control, we evaluated the binding specificity of the **TH59b-SL-PDS** to the construct **Tel-4G** (see Supplementary Figure S2D for sequence) in which the single-stranded G-quadruplex hosting DNA is flanked by a double-stranded section not recognized by the polyamides used here. Consistent with the **-1 nt telomere interface** without ligand (Figure 2B), this construct showed a mean rupture force of 21.1 ± 0.4 pN for the G-quadruplex formed in the ssDNA section in the same buffer (10 mM Tris with 100 mM KCl, pH 7.4) without ligand (Figure 3A). With 100 nM **TH59b-SL-PDS**, the G-quadruplex showed a ligand-bound fraction of 11.8% (Figure 3B), which is about 4 times lower than that in the **–1 nt telomere interface** con-

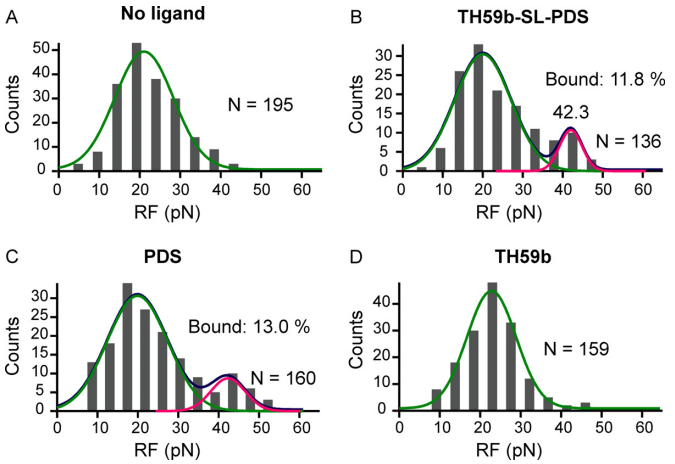

Figure 3. Interaction of the polyamide–pyridostatin (**TH59b-SL-PDS**), **TH59b**, and **PDS** with the G-quadruplex in the **Telo-4G** construct that contains duplex DNA sequences non-specific for the polyamide binding (see Supplementary Figure S2D for the construct sequence). The rupture force histograms of the Telo-4G construct are shown without ligand (**A**), and with 100 nM each of the **TH59b-SL-PDS** (**B**), **PDS** (**C**) or **TH59b** (**D**). The experiments were performed in a 10 mM Tris buffer (pH 7.4) with 100 mM KCl. The green solid curve depicts the ligand-free G-quadruplex whereas the pink solid curve represents the ligand-bound G-quadruplex. *N* represents the number of unfolding features.

struct (48.8%, Figure 2C). This result demonstrated that the dimeric tandem-hairpin polyamide moiety (**TH59b**) specifically interacts with the duplex telomeric sequence, facilitating the binding of the **TH59b-SL-PDS** to the **–1 nt telomere interface.** Compared to the **TH59b-SL-PDS** (11.8%), similar ligand-bound fraction (13.0%) (Figure 3C) was observed for the binding of 100 nM **PDS** to the Telo-4G, indicating that the polyamide moiety should not bind to the telomere G-quadruplex. This result was further confirmed by the absence of the binding between 100 nM polyamide **TH59b** and the telomere G-quadruplex in the Telo-4G construct (Figure 3D). All these control experiments firmly established the high binding specificity between the **TH59b-SL-PDS** and the natural telomere interface.

Submolecular dissection of the binding between the polyamide−pyridostatin conjugates and the telomere interface

As discussed above, the geometry of the mechanical unfolding described in Figure 1A cannot evaluate the binding of the polyamide (**TH59b**) to the telomere interface, which aligns with the direction of external force. As a result, it is impossible to directly compare the binding affinities of the **TH59b-SL-PDS** and the **TH59b** to the telomere interface. We reasoned that if the telomere interface can be introduced with an angle to the direction of mechanical unfolding, it becomes possible to evaluate the binding of the **TH59b** to the duplex region (51) as well as that of the **PDS** to the G-quadruplex. To this end, we introduced a DNA stem–loop structure (hairpin) in which duplex telomere sequence 5′-TAGGGTTAGGGTTAG is located in the hairpin stem whereas single-stranded $GG(TTAGGG)_3$ is placed in the loop (Figure 4A). Since this interface sequence is the same as the **-1 nt telomere interface**, the construct is named as '**-1 nt hairpin telomere interface**'. After the hairpin was tethered to the two optically trapped particles via two dsDNA handles, mechanical unfolding of the hairpin was carried out in a 10 mM Tris buffer supplemented with 100 mM KCl (pH 7.4).

Without ligands, two unfolding features were observed in *F–X* curves (Figure 4B green). The first feature at ∼15 pN is likely the unfolding of the DNA hairpin stem (52,53) whereas the second feature at ∼19 pN the unfolding of the telomere G-quadruplex (1) (Figure 4B green and Figure 4C top panel). Evaluation of the change-in-contour-length (ΔL) confirmed these assignments (observed ΔL: 26.0 ± 0.4 and 7.6 ± 0.2 nm for the hairpin and telomere G-quadruplex, respectively (Supplementary Figure S11 top panel); expected ΔL: ∼29.2 nm (hairpin) and ∼8.4 nm (G-quadruplex), see Supplementary Methods for calculation). During refolding, *F–X* curves showed two features without ligands. The first refolding feature appeared at ∼ 9.0 pN (Figure 4B, left curves). The rapid folding-unfolding transition (or hopping) at that force was indicative of hybridization and melting of the base pairs in the hairpin stem. Since G-quadruplex was located inside the loop of the hairpin (Figure 4A), the hybridization in any regime of the hairpin stem would mask the folding information of the G-quadruplex. The second refolding feature occurred at ∼4.5 pN, which indicated the folding to a fully folded hairpin (Figure 4B, left curves). The observed ΔL values for the first (13.3 ± 0.6 nm) and the second (15.6 ± 0.6 nm) refolding was close to that for a fully folded hairpin stem (37.6 nm, see Supplementary Method for calculation). The discrepancy can be due to the slow refolding transition between the two refolding events (Supplementary Figure S12). These observations strongly suggest the first refolding was due to the hybridization of the upper stem of the hairpin whereas the second refolding corresponded to the hybridization of the lower stem of the hairpin.

With these assignments, next, we mechanically unfolded the **–1 nt hairpin telomere interface** with 100 nM each of **PDS**, **TH59b** and **TH59b-SL-PDS** in the same Tris buffer. In **PDS**, the change-in-contour-lengths (ΔL) for the hairpin (25.6 ± 0.5 nm) and the G-quadruplex (7.6 ± 0.3 nm) were identical to those without ligand (Supplementary Figure S11, compare top 2 panels). However, we observed that some unfolding forces of the G-quadruplex increased from ∼19 pN to ∼40 pN (Figure 4C, curves see Supplementary Figure S11) whereas that of the hairpin did not change (Figures 4C). These results indicate that PDS specifically bound to a telomere G-quadruplex rather than the hairpin stem. After deconvolution of the unfolding force histograms, we obtained 14.3% ligand-bound G-quadruplex at 100 nM PDS.

In polyamide **TH59b**, we observed two different *F-X* curves (Supplementary Figure S11, Types III and IV) in addition to the curves identical to those without ligand (Supplementary Figure S11, Type I). In the Type III curve, the ΔL of the hairpin (27.0 ± 0.5 nm) or G-quadruplex (8.0 ± 0.2 nm) was similar to that without ligand (Supplementary Figure S11, compare the third and the top panels). While the unfolding force of hairpin increased, that of the G-quadruplex did not change (Figure 4C). These indicate

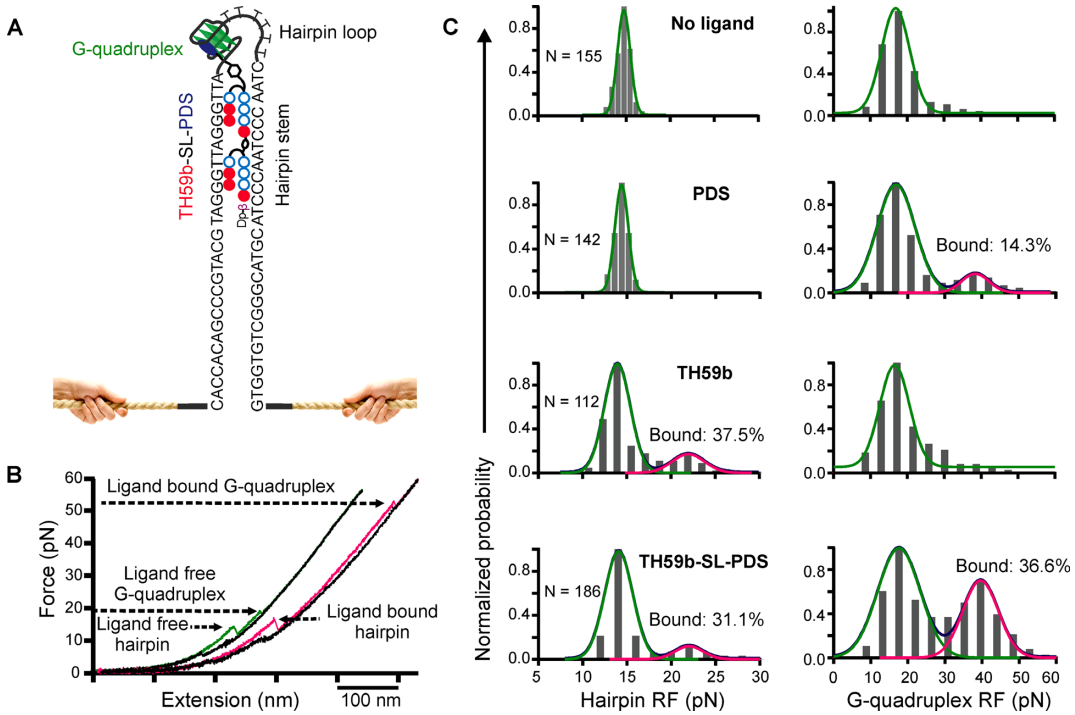

Figure 4. Binding evaluations of the **TH59b**, **PDS**, and **TH59b-SL-PDS** to the telomere interface contained in a stem-loop (hairpin) structure. (**A**) Schematic of the interaction between the **TH59b-SL-PDS** and the telomere interface (–1 nt spacer) inside the DNA hairpin (**-1 nt hairpin telomere interface**). The hairpin stem contains a TH59b binding sequence, whereas the hairpin loop contains telomere G-quadruplex sequence. The DNA hairpin is sandwiched between two dsDNA handles for mechanical unfolding experiments. (**B**) Representative force–extension curves without (green) and with 100 nM **TH59b-SL-PDS** (pink) recorded at ∼ 1.5 pN/s pulling rate. (**C**) Hairpin (left panels) and G-quadruplex (right panels) rupture force histograms without and with 100 nM each of the **PDS**, **TH59b**, or **TH59b-SL-PDS**. The green solid curve depicts the ligand-free G-quadruplex whereas the pink solid curve represents the ligand-bound G-quadruplex

that the polyamide specifically bound to the duplex hairpin stem instead of G-quadruplex. In the Type IV curves, three unfolding features were seen (Supplementary Figure S11). While the first two features are due to the stepwise unfolding of the hairpin stem as a result of the **TH59b** binding (see below), the third feature is for the G-quadruplex unfolding as evidenced by the unfolding force that is much higher than the hairpin and the ΔL (7.1 ± 0.2 nm, Supplementary Figure S11) that is consistent with the G-quadruplex (Supplementary Figure S11, top panel). Between the first two features, the lower-force feature is consistent with unfolding of the hairpin without ligand while the higher-force feature suggests the unfolding of a ligand-bound hairpin (Supplementary Figure S11, Type IV) (51). To confirm that the first two features of the Type IV curves are due to the stepwise unfolding of the hairpin, we summed the two ΔL values, which indeed showed a value (28.5 ± 0.5 nm) similar to that of the entire hairpin (Supplementary Figure S11, compare the top and the third panels). With the assignments of these unfolding features (first feature in the Type III and second feature in the Type IV curves), we were able to determine the TH59b-bound hairpin population as 37.5% in 100 nM **TH59b** (Figure 4C, third panel).

In conjugate **TH59b-SL-PDS**, we also observed ligand-bound (Figure 4B pink and Supplementary Figure S11) and ligand-free *F-X* curves (Supplementary Figure S11, Type I). Again, we observed that the ΔL values in TH59b-SL-PDS were similar to those without ligand (Supplementary Figure S11, compare the bottom and top panels), indicating hairpin and G-quadruplex form in presence of this ligand. As a bivalent binder, **TH59b-SL-PDS** can bind with the **–1 nt hairpin telomere interface** via either of the binding units (TH59b and PDS), or both. The unfolding features in the *F–X* curves should therefore reflect this scenario. However, we found majority of the binding occur via either the PDS unit (Supplementary Figure S11, Type II in the bottom panel) or both TH59b and PDS units (Supplementary Figure S11, Type V in the bottom panel) in the TH59b-SL-PDS, suggesting that PDS binding to the G-quadruplex is easier to occur than the TH59b binding to the duplex region. To determine PDS or TH59b bound fractions in the TH59-SL-PDS, we deconvoluted unfolding forces for the G-quadruplexes and hairpins separately (see Figure 4B pink and Figure 4C for unfolding force histograms). We found 31.1% and 36.6% bound populations as determined from the TH59b and the PDS bindings, respectively, in 100 nM **TH59b-SL-PDS**. To understand whether ligand binding can change the conformation of the G-quadruplex or hairpin structures as a function of force (54), we investigated RF vs ΔL plots for the **–1 nt telomere hairpin construct** without and with ligands (Supplementary Figure S13). In most cases, we did not observe strong force-dependent conformational change in G-quadruplex or hairpin in presence of ligands. In the two-step unfolding of the hairpin in presence of **TH59b** or **TH59b-SL-PDS**, we observed two corresponding

ΔL populations, each of which did not significantly vary with force.

Next, we evaluated the two refolding features of the **-1 nt hairpin telomere interface** with 100 nM each of **PDS**, **TH59b**, or **TH59b-SL-PDS** in the same Tris buffer. The first refolding force in presence of PDS was similar to that without ligand (∼9.0 pN) (Supplementary Figure S12). However, it increased to ∼9.4 pN in presence of TH59b or TH59b-SL-PDS (Supplementary Figure S12), which indicates that the TH59b may facilitate the folding of the upper stem region in which different hybridization matches exist in the presence of multiple TTAGGG repeats. The second refolding process showed the same force (∼4.5 pN) with and without each of the three ligands (Supplementary Figure S12). This is consistent with the folding of the lower stem of the hairpin in which no interaction is expected to exist between the hairpin and any of the ligand.

To compare the binding affinity of the PDS, TH59b or TH59b-SL-PDS ligands, we obtained rupture force histograms of the **-1 nt hairpin telomere interface** construct in the presence of 100–1000 nM for PDS, 10–500 nM for TH59b, and 1–100 nM for TH59b-SL-PDS (Figures 4C and Supplementary Figure S14). The ligand-bound hairpin or G-quadruplex fractions were then determined by statistical deconvolution (50) from the rupture force histograms described above. Binding curves were constructed based on the ligand-bound hairpin or G-quadruplex fractions vs different ligand concentrations. All binding curves follow Langmuir isotherms for single binding sites (Figure 5 A-D), which showed dissociation constant K_d of 440 ± 80 nM for the **PDS** (Figure 5A), 36 ± 7 nM for the **TH59b** (Figure 5B), and 0.8 ± 0.1 and 0.8 ± 0.2 nM for the **TH59b-SL-PDS** bindings (determined from the PDS and TH59b binding modes inside the TH59b-SL-PDS, respectively, see Figure 5C and D).

It is interesting that at saturating concentrations of these three ligands, only 40–50% of G-quadruplex/hairpin was bound to the ligand. This can be explained by two possible reasons. First, during force-ramping experiments before unfolding events, the increased tension experienced by the hairpin or G-quadruplex may slightly change their conformations, reducing their binding affinity with ligands. Second, there may be different G-quadruplex conformations formed in the interface construct, some of which may not bind well with ligands or the ligand binding may not substantially increase the unfolding force with respect to the ligand-free structures (55). In both cases, low-rupture force events misinterpreted as ligand-free states would be observed. It is necessary to point out that experiments in presence of all three ligands were performed under the same conditions (i.e. with the same maximum force and the same force-ramping rate). In addition, the saturation plateaus in presence of each of the three ligands also showed similar ligand-bound fractions. Therefore, the general trend of the K_d values should not vary significantly among the three ligands after considering these reasons.

The K_d of the PDS matches very well with the literature (1). It is only two times larger than that measured by SPR (K_d = 220 ± 40 nM, Supplementary Figure S15C). Such a difference is understandable given that the telomere interface construct was required to be placed closely to the surface in SPR and the construct was a little different from the single-molecule design (Supplementary Figure S2). These results confirm the accuracy of our new submolecular binding assays. The dissociation constants of the **TH59b-SL-PDS** to this **-1 nt hairpin telomere interface** construct (K_d = 0.8 nM) are also similar to that of the **–1 nt telomere interface** (K_d = 0.7 ± 0.1 nM), the **+1 nt telomere interface** (K_d = 1.2 ± 0.1 nM), or the **0 nt telomere interface** (K_d = 0.6 ± 0.1 nM) (determined from the PDS binding unit, see Supplementary Figure S16B–D), which again corroborates this new binding assay. It is significant that identical K_d values (0.8 nM) of the **TH59b-SL-PDS** were obtained from the PDS and TH59b binding components. This indicates that the sequential mechanical unfolding, which starts with the telomere duplex in the hairpin stem followed by telomere G-quadruplex in the hairpin loop, does not change the overall binding of the conjugate ligand.

However, K_d for the **TH59b-SL-PDS** in the SPR measurements (40 nM, Supplementary Figure S15D) is much higher than that observed in the optical tweezers experiments (0.8 nM, Figure 5C and D). The deviation can be explained by mis-paired structures that may exist in the SPR template (Supplementary Figure S17A). By pairing different $(TTAGGG)_2$ repeats with the C-rich complementary strands, these structures can interfere with correct G-quadruplex formation in the single-stranded section, reducing the overall affinity for the ligand conjugate. Since the mis-paired structures are not stable, they may induce breathing (53,56) in the duplex TTAGGG repeat. As a result, **TH59b-SL-PDS** shows much reduced binding affinity in the SPR interfacial construct. These artefacts in SPR experiments highlight the advantage of the K_d measurement by our mechanical unfolding method. First, the single-molecule template contains duplex handles, which ensure correct hybridization that leads to desired telomere interface without mis-paired species (Supplementary Figure S17B and C). Second, since only G-quadruplex and hairpin signals are measured mechanically, it excludes the interference from other regions, to which nonspecific ligand binding may occur. In addition, the single-molecule construct (Figure 1A) well mimics the natural telomere interface in which long duplex DNA is joined by ssDNA region section. Such an interface geometry is rather difficult to reproduce in the SPR experiments. Due to the requirement to place the telomere interface close to the SPR surface, the dsDNA section needs to be placed from the solution side of the interface, which may block the approach of ligands to the telomere interface.

TH59b-SL-PDS conjugate demonstrates stronger polymerase stop capability at the telomere interface than individual components

The K_d measurements indicate a significant increase (∼50 times compared to the TH59b and ∼500 times with respect to PDS) in the **TH59b-SL-PDS** binding to the telomere interface. Next, we set out to compare bioactivity of the **TH59b-SL-PDS** with respect to the individual components, **TH59b** or **PDS**. It is well known that G-quadruplex ligands can inhibit replication or transcription processes (40,57). With much increased binding affinity compared to

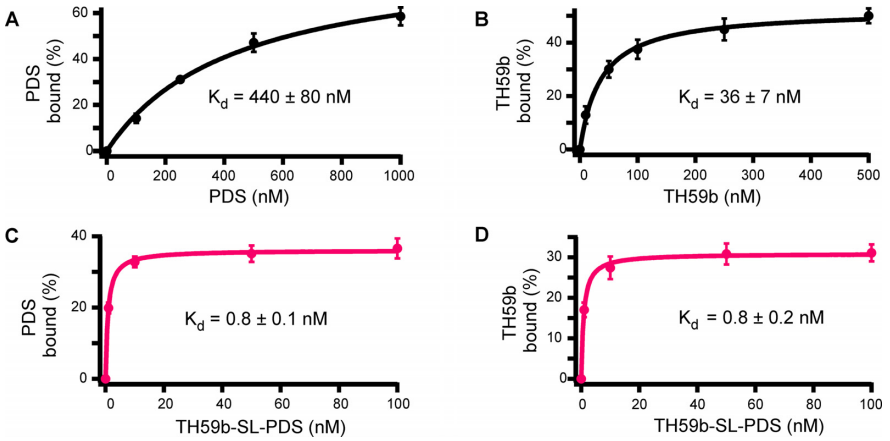

Figure 5. Measurements of the dissociation constants (K_d) for the **PDS** (**A**), **TH59b** (**B**) and **TH59b-SL-PDS** (**C**: from the PDS binding unit; **D**: from the TH59b binding unit) with **–1 nt hairpin telomere interface.**

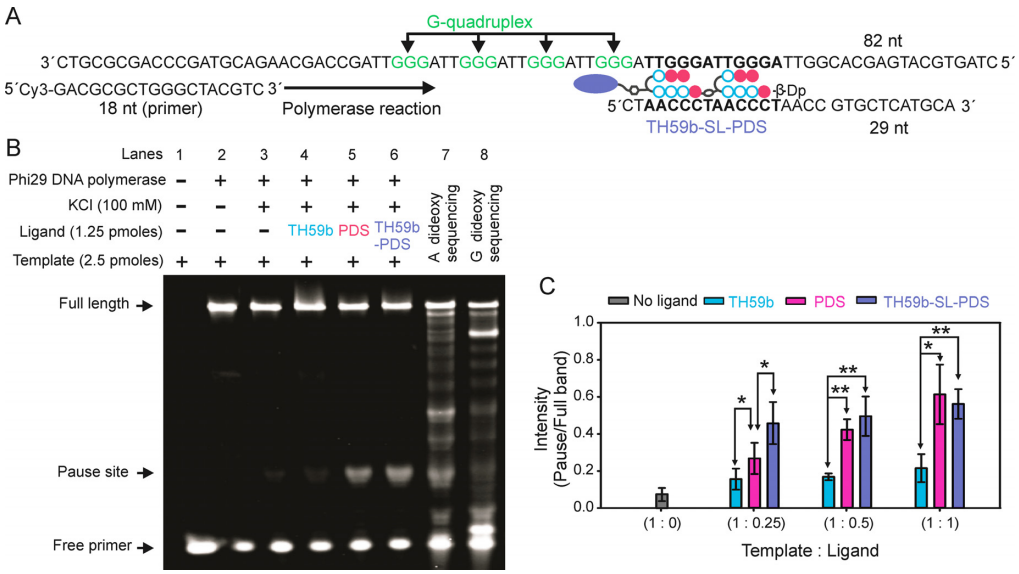

Figure 6. Polymerase stop assay of the **-1 nt telomere interface** with and without ligands. (**A**) The stop assay uses a DNA template in which the **–1 nt telomere interface** is placed downstream of a primer labelled with Cy3. (**B**) Denaturing PAGE gel analysis of the polymerase stop assay products in **TH59b**, **PDS**, and **TH59b-SL-PDS** (template: ligand = 1: 0.5). Positions of the full-length product, the pausing site corresponding to the interface, and the free primer are indicated. Lanes 7 and 8 represent dideoxy sequencing reactions. (**C**) Ratio (mean ± SD, $n = 3$) of the pause vs full product in presence of different ligands at various template versus ligand ratios. Single and double asterisks indicate significant differences at 90% and 95% confidence levels by *t* test, respectively.

the TH59b or PDS, we expect **TH59b-SL-PDS** may present stronger inhibitory effects. To test this hypothesis, we designed a DNA polymerase stop assay in which the **-1 nt telomere interface** was introduced downstream of a primer (Figure 6A).

Polymerase extension reaction was carried out using Phi29 DNA polymerase, a processive enzyme capable of displacing the non template DNA strand (58). First, we compared the replication stop patterns with and without 100 mM KCl. With KCl, the pausing site corresponding to the telomere interface was observed (Figure 6B, lane 3). As a control, the pausing did not show in the replication without KCl (lane 2). This indicates that formation of the G-quadruplex in the interface can partially stop the extension by Phi29 DNA polymerase.

To evaluate the replication stop effects of different ligands, the same stop assays were performed in presence of the TH59b, PDS and TH59b-SL-PDS ligands at 0.25–1 ligand versus template ratios (Figure 6B and C and Supplementary Figure S18A). The **TH59b-SL-PDS** showed the strongest pausing band, followed by **PDS** and **TH59b**, the latter of which showed the pausing pattern similar to that without ligands (Figure 6C). These results indicate that the polyamide–pyridostatin conjugate has the strongest replication stop effect. From the potency of the polymerase-stop effect, we also roughly estimated the dissociation constant (K_d), which showed a trend in qualitative agreement with single molecule measurements (K_d = 240 ± 80 nM for **PDS**, K_d = 50 ± 30 nM for **TH59b**, and K_d = 20 ± 10 nM for **TH59b-SL-PDS**, Supplementary Figure S18B).

It is noteworthy that at the 1:0.25 (template:ligand) ratio, the polyamide–pyridostatin ligand stopped replication much more efficiently than pyridostatin or polyamide. This again supports the strongest binding affinity of **TH59b-SL-PDS** among the three ligands. Even at low concentrations, **TH59b-SL-PDS** can bind efficiently to the telomere interface to stop the replication. When the ligand/template ratio increases, the difference in the replication stop for the three ligands becomes smaller, which is likely due to fact that binding of the TH59b and PDS to the telomere interface becomes saturated at higher concentrations.

CONCLUSIONS

In summary, we have synthesized new ligands (polyamide−pyridostatin) to target natural human telomere interfaces. By using innovative sub-molecular binding assays, we have demonstrated specific and high affinity binding of the dimeric tandem-hairpin polyamide−pyridostatin at the natural telomere interfaces. We obtained a K_d of 0.8 nM for the polyamide−pyridostatin conjugate **TH59b-SL-PDS**, which is ∼500 times stronger than the **PDS** binding to the telomere G-quadruplex and ∼50 times stronger than the TH59b binding to the telomere duplex. The strongest binding in **TH59b-SL-PDS** was corroborated by replication stop assays in which **TH59b-SL-PDS** demonstrated the strongest replication stop capability. The general strategy of conjugating highly specific duplex-binding molecules with G-quadruplex binders offers new guidelines to specifically target promoter G-quadruplexes, which are always flanked by duplex DNA. Since numerous activities are regulated by promoter G-quadruplexes, this dual targeting approach with high specificity and affinity is expected to address the major hurdle of side effects expected in current G-quadruplex ligands. On the other hand, the sub-molecular binding dissections can offer new perspectives to elucidate the binding mechanism of each monovalent component in a multivalent binding ligand.

SUPPLEMENTARY DATA

Supplementary Data are available at NAR Online.

FUNDING

National Science Foundation [CHE-1609514] (in part); National Institutes of Health [NIH 1R01CA236350–01A1] and National Natural Science Foundation of China [NSFC 21728801 to H.M.]; Basic Science and Platform Technology Program for Innovative Biological Medicine & JSPS-NSF International Collaborations in Chemistry (ICC) [JSPS KAKENHI 16H06356 to H.S., 15J00928 to Y.K.]. Funding for open access charge: National Science Foundation [CHE-1609514]; National Institutes of Health [NIH 1R01CA236350-01A1].
Conflict of interest statement. None declared.

REFERENCES

1. Koirala,D., Dhakal,S., Ashbridge,B., Sannohe,Y., Rodriguez,R., Sugiyama,H., Balasubramanian,S. and Mao,H. (2011) A single-molecule platform for investigation of interactions between G-quadruplexes and small-molecule ligands. *Nat. Chem.*, **3**, 782–787.
2. Yu,Z., Schonhoft,J.D., Dhakal,S., Bajracharya,R., Hegde,R., Basu,S. and Mao,H. (2009) ILPR G-Quadruplexes formed in seconds demonstrate high mechanical stabilities. *J. Am. Chem. Soc.*, **131**, 1876–1882.
3. Galburt,E.A., Grill,S.W., Wiedmann,A., Lubkowska,L., Choy,J., Nogales,E., Kashlev,M. and Bustamante,C. (2007) Backtracking determines the force sensitivity of RNAP II in a factor-dependent manner. *Nature*, **446**, 820–823.
4. Mejia,Y.X., Mao,H., Forde,N.R. and Bustamante,C. (2008) Thermal probing of E. coli RNA polymerase off-pathway mechanisms. *J. Mol. Biol.*, **382**, 628–637.
5. Wang,M.D., Schnitzer,M.J., Yin,H., Landick,R., Gelles,J. and Block,S.M. (1998) Force and velocity measured for single molecules of RNA polymerase. *Science*, **282**, 902–907.
6. Li,J.-L., Harrison,R.J., Reszka,A.P., Brosh,R.M., Bohr,V.A., Neidle,S. and Hickson,I.D. (2001) Inhibition of the Bloom's and Werner's syndrome helicases by G-Quadruplex interacting ligands. *Biochemistry*, **40**, 15194–15202.
7. Han,H., Bennett,R. and Hurley,L. (2000) Inhibition of Unwinding of G-Quadruplex Structures by Sgs1 Helicase in the Presence of N,N'-Bis[2-(1-piperidino)ethyl]-3,4,9,10-perylenetetracarboxylic Diimide, a G-Quadruplex-Interactive Ligand. *Biochemistry*, **39**, 9311–9316.
8. Liu,J.-q., Chen,C.-y., Xue,Y., Hao,Y.-h. and Tan,Z. (2010) G-Quadruplex hinders translocation of BLM helicase on DNA: a real-time fluorescence spectroscopic unwinding study and comparison with duplex substrates. *J. Am. Chem. Soc.*, **132**, 10521–10527.
9. Rodriguez,R., Muüller,S., Yeoman,J.A., Trentesaux,C., Riou,J.-F. and Balasubramanian,S. (2008) A novel small molecule that alters shelterin integrity and triggers a DNA-Damage Response at telomeres. *J. Am. Chem. Soc.*, **130**, 15758–15759.
10. Tauchi,T., Shin-ya,K., Sashida,G., Sumi,M., Nakajima,A., Shimamoto,T., Ohyashiki,J.H. and Ohyashiki,K. (2003) Activity of a novel G-quadruplex-interactive telomerase inhibitor, telomestatin (SOT-095), against human leukemia cells: involvement of ATM-dependent DNA damage response pathways. *Oncogene*, **22**, 5338–5347.
11. Burger,A.M., Dai,F.P., Schultes,C.M., Reszka,A.P., Moore,M.J., Double,J.A. and Neidle,S. (2005) The G-quadruplex-interactive molecule BRACO-19 inhibits tumor growth, consistent with telomere targeting and interference with telomerase function. *Cancer Res.*, **65**, 1489–1496.
12. Zhou,J.-L., Lu,Y.-J., Ou,T.-M., Zhou,J.-M., Huang,Z.-S., Zhu,X.-F., Du,C.-J., Bu,X.-Z., Ma,L., Gu,L.-Q *et al.*2005) Synthesis and evaluation of quindoline derivatives as G-Quadruplex inducing and stabilizing ligands and potential inhibitors of telomerase. *J. Med. Chem.*, **48**, 7315–7321.
13. Huppert,J.L. and Balasubramanian,S. (2005) Prevalence of quadruplexes in the human genome. *Nucleic Acids Res.*, **33**, 2908–2916.
14. Chambers,V.S., Marsico,G., Boutell,J.M., Di Antonio,M., Smith,G.P. and Balasubramanian,S. (2015) High-throughput sequencing of DNA G-quadruplex structures in the human genome. *Nat. Biotech.*, **33**, 877–881.
15. Huppert,J.L., Bugaut,A., Kumari,S. and Balasubramanian,S. (2008) G-quadruplexes: the beginning and end of UTRs. *Nucleic Acids Res.*, **36**, 6260–6268.
16. Punnoose,J.A., Ma,Y., Li,Y., Sakuma,M., Mandal,S., Nagasawa,K. and Mao,H. (2017) Adaptive and specific recognition of telomeric G-Quadruplexes via Polyvalency induced unstacking of binding units. *J. Am. Chem. Soc.*, **139**, 7476–7484.
17. Asamitsu,S., Obata,S., Phan,A.T., Hashiya,K., Bando,T. and Sugiyama,H. (2018) Simultaneous binding of hybrid molecules constructed with dual DNA-Binding components to a G-Quadruplex and its proximal duplex. *Chemistry*, **24**, 4428–4435.
18. Nguyen,T.Q.N., Lim,K.W. and Phan,A.T. (2017) A dual-specific targeting approach based on the simultaneous recognition of duplex and quadruplex motifs. *Sci Rep*, **7**, 11969.
19. Mammen,M., Choi,S.-K. and Whitesides,G.M. (1998) Polyvalent interactions in biological systems: implications for design and use of multivalent ligands and inhibitors. *Angew. Chem. Int. Ed. Engl.*, **37**, 2754–2794.

20. Mandal,S., Selvam,S., Shrestha,P. and Mao,H. (2016) Mechanochemical sensing of single and few Hg(II) ions using polyvalent principles. *Anal. Chem.*, **88**, 9479–9485.
21. Dervan,P.B. and Burli,R.W. (1999) Sequence-specific DNA recognition by polyamides. *Curr. Opin. Chem. Biol.*, **3**, 688–693.
22. White,S., Szewczyk,J.W., Turner,J.M., Baird,E.E. and Dervan,P.B. (1998) Recognition of the four Watson-Crick base pairs in the DNA minor groove by synthetic ligands. *Nature*, **391**, 468–471.
23. de Clairac,R.P.L., Geierstanger,B.H., Mrksich,M., Dervan,P.B. and Wemmer,D.E. (1997) NMR characterization of hairpin polyamide complexes with the minor groove of DNA. *J. Am. Chem. Soc.*, **119**, 7909–7916.
24. Herman,D.M., Turner,J.M., Baird,E.E. and Dervan,P.B. (1999) Cycle polyamide motif for recognition of the minor groove of DNA. *J. Am. Chem. Soc.*, **121**, 1121–1129.
25. Herman,D.M., Baird,E.E. and Dervan,P.B. (1999) Tandem hairpin motif for recognition in the Minor groove of DNA by pyrrole–Imidazole polyamides. *Chemistry*, **5**, 975–983.
26. Blackburn,E.H. (1991) Structure and function of telomeres. *Nature*, **350**, 569–573.
27. Chan,S.R.W.L. and Blackburn,E.H. (2004) Telomeres and telomerase. *Philos. Trans. Roy. Soc. London B: Biol Sci*, **359**, 109–122.
28. Moyzis,R.K., Buckingham,J.M., Cram,L.S., Dani,M., Deaven,L.L., Jones,M.D., Meyne,J., Ratliff,R.L. and Wu,J.-R. (1988) A highly conserved repetitive DNA sequence, (TTAGGG)n, present at the telomeres of human chromosomes. *Proc. Natl. Acad. Sci. U.S.A.*, **85**, 6622–6626.
29. Wright,W.E., Tesmer,V.M., Huffman,K.E., Levene,S.D. and Shay,J.W. (1997) Normal human chromosomes have long G-rich telomeric overhangs at one end. *Genes Dev.*, **11**, 2801–2809.
30. Russo Krauss,I., Ramaswamy,S., Neidle,S., Haider,S. and Parkinson,G.N. (2016) Structural insights into the Quadruplex-Duplex 3′ interface formed from a telomeric repeat: a potential molecular target. *J. Am. Chem. Soc.*, **138**, 1226–1233.
31. Mao,H. and Luchette,P. (2008) An integrated laser-tweezers instrument for microanalysis of individual protein aggregates. *Sens. Actuators B*, **129**, 764–771.
32. Baumann,C.G., Smith,S.B., Bloomfield,V.A. and Bustamante,C. (1997) Ionic effects on the elasticity of single DNA molecules. *Proc. Natl. Acad. Sci. U.S.A.*, **94**, 6185–6190.
33. Yu,Z. and Mao,H. (2013) Non-B DNA structures show diverse conformations and complex transition kinetics comparable to RNA or proteins | a perspective from mechanical unfolding and refolding experiments. *Chem. Rec.*, **13**, 102–116.
34. Dhakal,S., Cui,Y., Koirala,D., Ghimire,C., Kushwaha,S., Yu,Z., Yangyuoru,P.M. and Mao,H. (2013) Structural and mechanical properties of individual human telomeric G-quadruplexes in molecularly crowded solutions. *Nucleic Acids Res.*, **41**, 3915–3923.
35. Hirata,A., Nokihara,K., Kawamoto,Y., Bando,T., Sasaki,A., Ide,S., Maeshima,K., Kasama,T. and Sugiyama,H. (2014) Structural evaluation of tandem hairpin Pyrrole–Imidazole polyamides recognizing human telomeres. *J. Am. Chem. Soc.*, **136**, 11546–11554.
36. Kawamoto,Y., Sasaki,A., Chandran,A., Hashiya,K., Ide,S., Bando,T., Maeshima,K. and Sugiyama,H. (2016) Targeting 24 bp within telomere repeat sequences with tandem tetramer Pyrrole–Imidazole polyamide probes. *J. Am. Chem. Soc.*, **138**, 14100–14107.
37. Kawamoto,Y., Sasaki,A., Hashiya,K., Ide,S., Bando,T., Maeshima,K. and H.,S. (2015) Tandem trimer pyrrole–imidazole polyamide probes targeting 18 base pairs in human telomere sequences. *Chem. Sci.*, **6**, 2307–2312.
38. Read,M., Harrison,R.J., Romagnoli,B., Tanious,F.A., Gowan,S.H., Reszka,A.P., Wilson,W.D., Kelland,L.R. and Neidle,S. (2001) Structure-based design of selective and potent G quadruplex-mediated telomerase inhibitors. *Proc. Natl. Acad. Sci. U.S.A.*, **98**, 4844–4849.
39. Sun,D. and Hurley,L.H. (2010) Biochemical techniques for the characterization of G-quadruplex structures: EMSA, DMS footprinting, and DNA polymerase stop assay. *Methods Mol. Biol.*, **608**, 65–79.
40. Han,H., Hurley,L.H. and Salazar,M. (1999) A DNA polymerase stop assay for G-quadruplex-interactive compounds. *Nucleic Acids Res.*, **27**, 537–542.
41. Kawamoto,Y., Bando,T., Kamada,F., Li,Y., Hashiya,K., Maeshima,K. and Sugiyama,H. (2013) Development of a new method for synthesis of tandem hairpin pyrrole-imidazole polyamide probes targeting human telomeres. *J Am Chem Soc*, **135**, 16468–16477.
42. Maeshima,K., Janssen,S. and Laemmli,U.K. (2001) Specific targeting of insect and vertebrate telomeres with pyrrole and imidazole polyamides. *EMBO J.*, **20**, 3218–3228.
43. Sasaki,A., Ide,S., Kawamoto,Y., Bando,T., Murata,Y., Shimura,M., Yamada,K., Hirata,A., Nokihara,K., Hirata,T *et al.*2016) Telomere visualization in tissue sections using Pyrrole-Imidazole polyamide probes. *Sci. Rep.*, **6**, 29261.
44. Sfeir,A.J., Chai,W., Shay,J.W. and Wright,W.E. (2005) Telomere-end processing. *Mol. Cell*, **18**, 131–138.
45. Ambrus,A., Chen,D., Dai,J., Bialis,T., Jones,R.A. and Yang,D. (2006) Human telomeric sequence forms a hybrid-type intramolecular G-quadruplex structure with mixed parallel/antiparallel strands in potassium solution. *Nucleic Acids Res.*, **34**, 2723–2735.
46. Phan,A.T., Kuryavyi,V., Luu,K.N. and Patel,D.J. (2007) Structure of two intramolecular G-quadruplexes formed by natural human telomere sequences in K+ solution. *Nucleic Acids Res.*, **35**, 6517–6525.
47. Yu,Z., Koirala,D., Cui,Y., Easterling,L.F., Zhao,Y. and Mao,H. (2012) Click chemistry assisted single-molecule fingerprinting reveals a 3D biomolecular folding funnel. *J. Am. Chem. Soc.*, **134**, 12338–12341.
48. Rodriguez,R., Miller,K.M., Forment,J.V., Bradshaw,C.R., Nikan,M., Britton,S., Oelschlaegel,T., Xhemalce,B., Balasubramanian,S. and Jackson,S.P. (2012) Small-molecule–induced DNA damage identifies alternative DNA structures in human genes. *Nat. Chem. Biol.*, **8**, 301–310.
49. Gavathiotis,E., Heald,R.A., Stevens,M.F.G. and Searle,M.S. (2001) Recognition and stabilization of quadruplex DNA by a potent new telomerase Inhibitor: NMR studies of the 2:1 complex of a pentacyclic methylacridinium cation with d(TTAGGGT)4. *Angew. Chem. Int. Ed. EngI.*, **113**, 4885–4887.
50. Dhakal,S., Schonhoft,J.D., Koirala,D., Yu,Z., Basu,S. and Mao,H. (2010) Coexistence of an ILPR i-Motif and a partially folded structure with comparable mechanical stability revealed at the single-molecule level. *J. Am. Chem. Soc.*, **132**, 8991–8997.
51. Camunas-Soler,J., Alemany,A. and Ritort,F. (2017) Experimental measurement of binding energy, selectivity, and allostery using fluctuation theorems. *Science*, **355**, 412–415.
52. Mandal,S., Koirala,D., Selvam,S., Ghimire,C. and Mao,H. (2015) A molecular tuning fork in single-molecule mechanochemical sensing. *Angew. Chem. Int. Ed. Engl.*, **54**, 7607–7611.
53. Woodside,M.T., Behnke-Parks,W.M., Larizadeh,K., Travers,K., Herschlag,D. and Block,S.M. (2006) Nanomechanical measurements of the sequence-dependent folding landscapes of single nucleic acid hairpins. *Proc. Natl. Acad. Sci. U.S.A.*, **103**, 6190–6195.
54. Zhong,Z., Soh,L.H., Lim,M.H. and Chen,G. (2015) A U·U Pair-to-U·C pair Mutation-Induced RNA native structure destabilisation and Stretching-Force-Induced RNA misfolding. *Chem. Plus Chem.*, **80**, 1267–1278.
55. Jonchhe,S., Ghimire,C., Cui,Y., Sasaki,S., McCool,M., Park,S., Iida,K., Nagasawa,K., Sugiyama,H. and Mao,H. (2019) Binding of a telomestatin derivative changes mechanical anisotropy of human telomeric G-Quadruplex. *Angew. Chem. Int. Ed. Engl.*, **58**, 877–881.
56. von Hippel,P.H., Johnson,N.P. and Marcus,A.H. (2013) 50 years of DNA 'Breathing': reflections on old and new approaches. *Biopolymers*, **99**, 923–954.
57. Siddiqui-Jain,A., Grand,C.L., Bearss,D.J. and Hurley,L.H. (2002) Direct evidence for a G-quadruplex in a promoter region and its targeting with a small molecule to repress c-*MYC* transcription. *Proc. Natl. Acad. Sci. U.S.A.*, **99**, 11593–11598.
58. Dean,F.B., Nelson,J.R., Giesler,T.L. and Lasken,R.S. (2001) Rapid amplification of plasmid and phage DNA using Phi29 DNA polymerase and multiply-primed rolling circle amplification. *Genome Res.*, **11**, 1095–1099.